Originally published as:

Geophysical Journal International

The influence of crustal scattering on translational and rotational motions in regional and teleseismic coda waves

Peter J. Gaebler,[1,2] Christoph Sens-Schönfelder[1] and Michael Korn[2]

[1]*GFZ German Research Centre for Geosciences, Section* 2.4, *Telegrafenberg, D*-14473 *Potsdam, Germany. E-mail:* peter.gaebler@bgr.de
[2]*Institute for Geophysics and Geology, University of Leipzig, Talstraße* 35, *D*-04103 *Leipzig, Germany*

SUMMARY

Monte Carlo solutions to the radiative transfer equations are used to model translational and rotational motion seismogram envelopes in random elastic media with deterministic background structure assuming multiple anisotropic scattering. Observation and modelling of the three additional components of rotational motions can provide independent information about wave propagation in the Earth's structure. Rotational motions around the vertical axis observed in the *P*-wave coda are of particular interest as they can only be excited by horizontally polarized shear waves and therefore indicate the conversion from *P* to *SH* energy by multiple scattering at 3-D heterogeneities. To investigate crustal scattering and attenuation parameters in south-east Germany beneath the Gräfenberg array multicomponent seismogram envelopes of rotational and translational motions are synthesized and compared to seismic data from regional swarm-earthquakes and of deep teleseismic events. In the regional case a nonlinear genetic inversion is used to estimate scattering and attenuation parameters at high frequencies (4–8 Hz). Our preferred model of crustal heterogeneity consists of a medium with random velocity and density fluctuations described by an exponential autocorrelation function with a correlation length of a few hundred metres and fluctuations in the range of 3 per cent. The quality factor for elastic *S*-waves attenuation Q_i^S is around 700. In a second, step simulations of teleseismic *P*-wave arrivals using this estimated set of scattering and attenuation parameters are compared to observed seismogram envelopes from deep events. Simulations of teleseismic events with the parameters found from the regional inversion show good agreement with the measured seismogram envelopes. This includes ringlaser observations of vertical rotations in the teleseismic *P*-wave coda that naturally result from the proposed model of wave scattering. The model also predicts, that the elastic energy recorded in the teleseismic *P* coda is not equipartitioned, unlike the coda of regional events, but contains an excess of shear energy. The results confirm that scattering generating the teleseismic *P*-wave coda mainly occurs in the crustal part of the lithosphere beneath the receiver. Our observations do not require scattering of high frequency waves in the mantle, but weak scattering in the lithospheric mantle cannot be ruled out.

Key words: Numerical solutions; Earthquake ground motions; Seismic attenuation; Statistical seismology; Wave scattering and diffraction; Wave propagation.

1 INTRODUCTION

The purpose of this study is to evaluate the contribution of local crustal heterogeneity to the generation of scattered elastic energy recorded in various seismic signals. Of specific interest in this context are records of rotational ground motions that, acting as a polarization filter for shear energy, can provide additional information about conversion scattering that couples *P*- and *S*-wave propagation. The strategy we follow starts with a conventional inversion of seismogram envelopes from regional earthquakes for the local

scattering and attenuation properties of the crust in southeast Germany. In a second step we test whether the medium heterogeneity, described by these parameters, is suitable to generate seismogram envelopes of teleseismic earthquakes. For this we simulate seismogram envelopes of *P*-wave coda from deep teleseismic earthquakes including rotational motions and compare these to ringlaser recordings of the vertical rotation rate and usual translational seismograms. As this study is based on the analysis of the seismic coda, we start off with a short introduction on scattered energy in the seismic coda in Section 1.1, followed by an overview of previous investigations

on crustal wave scattering and attenuation in Section 1.2. As we additionally use rotational motions, basic information about that topic can be found in Section 1.3. Section 2 introduces radiative transfer theory (RTT), its solutions and the modelling of translational and rotational seismogram envelopes from regional and teleseismic events. Details about the study area and data can be found in Section 3. The inversion approach and its results using records from regional events is described in Section 4. Based on these parameters we present in Section 5 the results of the modelling of rotational and translational ground motions of teleseismic arrivals and their comparison to a set of records from four deep earthquakes at an epicentral distance of about 70°. Results are discussed and interpreted in Section 6.

1.1 Scattered energy in the seismic coda

Since the early 1970s the observation, analysis and interpretation of coda waves is receiving attention in the field of seismology. According to Aki (1969) the seismic coda can be referred to as seismic energy recorded after the passage of the primary seismic waves and can be explained with the scattering of seismic waves at randomly distributed small scale heterogeneities in the subsurface (Aki & Chouet 1975). The energy decay of the seismic coda with time depends on the investigated frequency band and is a local property of the subsurface. Parameters such as source mechanism, epicentral distance, magnitude, event depth or source orientation show minor influence on the energy decay in the seismic coda (Trégourès *et al.* 2002). Therefore many studies relate physical properties of the subsurface to the observed local or regional seismic coda signals (Aki 1969; Abubakirov & Gusev 1990; Calvet & Margerin 2013). Total attenuation Q_t is not only due to anelastic attenuation measured by the intrinsic quality factor Q_i, but is a combination of intrinsic attenuation and amplitude decrease due to redistribution of energy by scattering described by the quality factor Q_s (Aki 1981; Dainty 1981; Toksöz *et al.* 1988). The decay of the coda amplitude is expressed in analogy to a quality factor by the coda-Q parameter Q_c. Apparent or total attenuation Q_t is therefore given by:

$$\frac{1}{Q_t} = \frac{1}{Q_i} + \frac{1}{Q_s}. \qquad (1)$$

The spatial scale of the heterogeneity that interacts with the wavefield to generate the scattered part is below the resolution limits of imaging techniques prohibiting a deterministic description. Instead it is possible to regard the heterogeneity as a continuous random medium where the medium properties like, for example density ρ are given as $\rho(\mathbf{x}) = \rho_0[1 + \xi(\mathbf{x})]$ with ρ_0 being the average background value and $\xi(\mathbf{x})$ describing its random fluctuations. The fluctuations are described by their statistical properties that are often defined using the autocorrelation function (ACF) R. In a statistically homogeneous isotropic medium the ACF only depends on the absolute value of distance $r = |\mathbf{r}|$ between two points. Such ACFs are mainly characterized by two parameters, the fluctuation strength ϵ and the correlation length a. The fluctuation strength ϵ is a measure of amplitude of the velocity or density fluctuations around their background value. The correlation length a gives information about the length scale of the fluctuations. For numerical modelling the medium fluctuations are usually described by their power spectral density (PSD) function which is the Fourier-transform of the ACF. The most commonly used random media have gaussian, exponential or von Karman type ACFs (Sato *et al.* 2012). Gaussian ACFs are used to describe relatively smooth random media with fluctuations of similar size. A wide range of random media with

small scale fluctuations is described by the von Karman ACF. Additional to the fluctuation strength ϵ and correlation length a, a third parameter ν describes the roll-off of the amplitude of fluctuations at high wavenumbers, which governs the roughness of the medium. Here we use a random medium with exponential ACF which is a special case of the von Karman medium with moderate roughness expressed by $\nu = 0.5$. The exponential ACF $R_e(r)$ and the corresponding PSD function $P_e(m)$ are defined as

$$R_e(r) = \epsilon^2 e^{-r/a} \qquad (2)$$

$$P_e(m) = \frac{8\pi\epsilon^2 a^3}{(1 + a^2 m^2)^2}, \qquad (3)$$

with m being the wavenumber. Other parameters to describe the strength of scattering in the Earth's crust are the mean free path l and the transport mean free path l^*. Mean free path l is a measure of the characteristic distance between two scattering events, the transport mean free path l^* can be regarded as the propagation distance required for a wave to lose memory of its initial direction.

Several methods were proposed to model the generation of seismic coda due to scattering at statistically distributed heterogeneities in the subsurface (Sato *et al.* 2012). One of the simplest approaches to simulate the energy in the seismic coda assumes single isotropic scattering of acoustic energy and was for example described by Sato (1977). Single scattering theory assumes that seismic waves are scattered only once between source and receiver. Scattering events in this model are supposed to be isotropic, which means there is no preferred direction of scattering of the energy. The scattering of S waves is treated in the limits of the acoustical approximation. Scattering of P waves and conversion scattering between S and P energy is not included in this theory. One possible method to model the propagation of seismic energy in such a scattering medium is the RTT. Details of this theory and possible solutions are discussed in Section 2. A variety of studies make use of the diffusion approximation (Dainty *et al.* 1974; Aki & Chouet 1975; Dainty 1981) to model the coda. This approach assumes strong scattering and is only valid for long lapse times. Other studies clearly show the importance of multiple scattering of the seismic wavefield at heterogeneities in the Earth's subsurface (Wu 1985; Wu & Aki 1988; Abubakirov & Gusev 1990; Hoshiba *et al.* 1991; Margerin *et al.* 2000; Wegler & Lühr 2001; Sens-Schönfelder *et al.* 2009). Abubakirov & Gusev (1990) and Hoshiba (1995) introduced the theory of anisotropic scattering. The modelling of elastic energy allows to model P and S energy as well as conversion processes between these modes. Multiple elastic scattering was for example modelled by Margerin *et al.* (2000) using randomly distributed spheres in an otherwise homogeneous background medium. This theory was extended to a medium with continuous random inhomogeneities (Przybilla *et al.* 2006). Sens-Schönfelder *et al.* (2009) describe an algorithm based on RTT to model seismogram envelopes for multiple anisotropic scattering of elastic waves at randomly distributed heterogeneities in a deterministic macroscopic background structure. This method is able to model not only the coda, but also the envelopes of the direct onsets of the primary waves.

1.2 Previous investigations of crustal wave scattering and attenuation

Scattering and attenuation parameters of the crust in different regions worldwide have been subject of numerous studies using a broad range of data sets, models and methods. Inhomogeneities in volcanic areas can be very strong and the mean free path length

Table 1. Comparison of crustal attenuation and scattering parameters for different study areas.

Reference	Region	Distance	f_c (Hz)	Q_i^{S-1}	l (km)	l^* (km)	ϵ (per cent)	a (km)
Abubakirov & Gusev (1990)	Kamchatka	Local	3	0.0032	150	–	–	–
Fehler *et al.* (1992)	Japan	Local	3	0.0026	150	–	–	–
Rothert (2000)	Germany	Teleseismic	2	–	–	–	3–7	0.6–4.8
Lacombe *et al.* (2003)	France	Regional	3	0.0013	250	250	–	–
Sens-Schönfelder & Wegler (2006)	Germany	Regional	3	0.0013	690	690	–	–
Przybilla *et al.* (2009)	Norway	Local	3	–	175	250	–	–
Sens-Schönfelder *et al.* (2009)	France	Regional	3	0.0016	–	761	2.1	0.77
Calvet & Margerin (2013)	France	Local	6	0.0013	>80	400	3.7	0.16
This study	Germany	Regional + tele	6	0.0015	290	420	2.9	0.27

can reach values from as low as 0.1 to 150 km (Abubakirov & Gusev 1990; Fehler *et al.* 1992; Wegler & Lühr 2001). Areas with continental crust generally show weaker scattering than volcanic areas. In our study area in Germany Sens-Schönfelder & Wegler (2006) used an acoustic and isotropic scattering model to estimate a transport mean free path length of 690 km and an intrinsic Q value for S waves Q_i^S of 769 at 3 Hz. A further investigation by Sens-Schönfelder *et al.* (2009) in France using an elastic multiple anisotropic scattering approximation resulted in a transport mean free path of 761 km and Q_i^S of 625 at 3 Hz. A study by Rothert (2000) is of special interest here, as it covers a similar region as our investigation, the area of the Gräfenberg array in southeast Germany. Wave fronts from teleseismic P-wave arrivals were analysed to describe the heterogeneities in the subsurface. A random medium with velocity fluctuations of 3–7 per cent and correlation lengths of 0.6–4.8 km is proposed to describe the heterogeneities. Hock *et al.* (2004) found values of 1–2.5 km for a and 4–5 per cent for ϵ in the same area. Similar values for crustal scattering have for example been found by Levander *et al.* (1994) or Calvet & Margerin (2013). A comparison of crustal attenuation and scattering parameters from selected study areas is given in Table 1. For a more complete review on investigations of crustal wave scattering we refer the reader to Sato *et al.* (2012).

1.3 Rotational motions in seismology

To give a full description of the seismic wavefield, the measurement of three components of translational motion, six components of strain and three components of rotational motion is necessary (Aki & Richards 2002). Translations and strains have routinely been used for a long time to record the seismic wavefield. The three components of translational ground displacement (ground velocity or acceleration) are measured using inertial seismometers. Additionally it is possible to record deformations in the Earth using strainmeters. The third quantity, the three components of rotational motion, on the other hand is extremely hard to measure, mainly due to low sensitivity of the instruments. The development of high sensitivity rotational motion sensors such as ring laser gyroscopes makes it nowadays possible to record the rotational motions in the seismic wavefield induced by earthquakes (Igel *et al.* 2007) and even by ambient seismic noise (Hadziioannou *et al.* 2012). In this study, we use the ringlaser rotation sensor located at the geodetic Fundamentalstation in Wettzell, Germany. The ringlaser is an active interferometer with two laser beams circulating around a closed cavity in opposite directions. The Sagnac beat frequency δf of the two light beams is given as

$$\delta f = \frac{4A(\mathbf{n} \cdot \dot{\Omega})}{\lambda P}, \tag{4}$$

with A being the area within the laser ring, n the surface normal, $\dot{\Omega}$ the rotation rate, λ the wavelength of the laser and P being the perimeter of the instrument. As an optical instrument the sensor has a flat response over the entire frequency range which allows simultaneous observations of the Earth's rotation and seismic waves. A change of the beat frequency can be caused by several effects (Igel *et al.* 2005). First, variations of the scaling factor $A/\lambda P$ will change the beat frequency, an effect that is minimized by temperature and pressure shielding and extremely low expansion coefficients of the device. Another reason for variations in δf are changes in the surface normal $\mathbf{n}$ of the ringlaser with respect to the rotation axis. These variations may be caused for example by solid Earth tides, ocean loading (Schreiber *et al.* 2009) or diurnal polar motions (Schreiber *et al.* 2004). The third reason for variations in δf are changes in $\dot{\Omega}$, that is changes in the rotation rate itself. These variations are caused by changes in the Earth's rotation rate as a consequence of mass redistributions or may also be seismically induced. For a more detailed description of the Wettzell ringlaser, we refer to Schreiber *et al.* (2009). For rotational motion sensor examples and more details on rotational motions see, for example McLeod & Stedman (1998), Pancha *et al.* (2000) and Brokešová *et al.* (2012). Earthquake induced rotational motions over a wide range of magnitudes and epicentral distances are reported by Igel *et al.* (2005, 2007). Records of rotational motions can find use in several applications. Bernauer *et al.* (2009) introduced a technique to incorporate rotational motions into the seismic inverse problem to improve tomographic images in the vicinity of seismic stations. Another application using rotational motions is the determination of seismic phase velocities and source directions from point measurements using collocated observations of rotational motions and translational accelerations induced by earthquakes (Igel *et al.* 2007; Kurrle *et al.* 2010) or ambient seismic noise (Hadziioannou *et al.* 2012). Igel *et al.* (2007) and Pham *et al.* (2009b) report direct observations of rotational motions around the vertical axis in the coda of the direct teleseismic P waves. A local and a teleseismic example for rotational motions around the vertical axis recorded at the Fundamentalstation Wettzell in southeast Germany is shown in Fig. 1. This observation is of particular interest for our study as rotational motions around the vertical axis are not sensitive to compressional waves and are only excited by horizontally polarized shear waves. Igel *et al.* (2007) pointed out, that P and Rayleigh waves at the Earth's surface can lead to tilting effects and therefore pollute the rotational motion. The tilt signal can be estimated roughly from the vertical translational motions, but its contribution to the rotations is small in comparison to the noise of the rotational sensor (Pham *et al.* 2009a) and far below the detected signal. Another possible explanation for the observed rotations is the conversion of P to SH energy at 3-D heterogeneities close to the receiver. This conversion processes will be used in the paper to
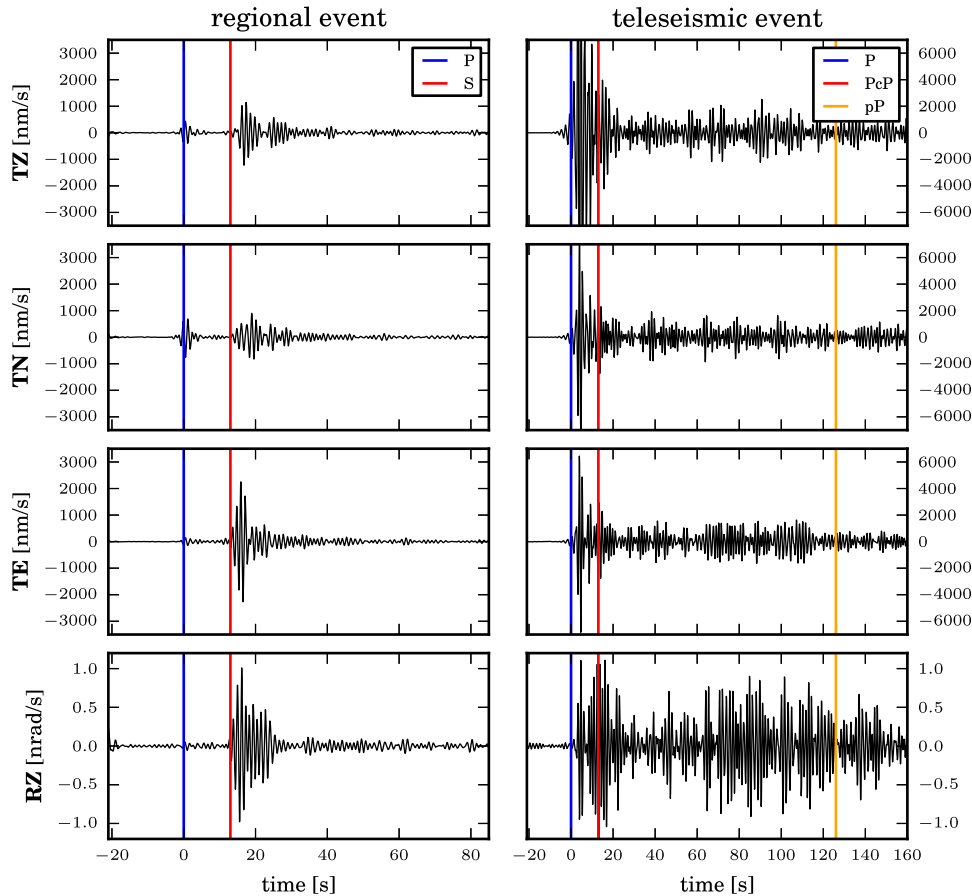
Figure 1. Example for rotational motions. Top three traces show measured ground velocities in vertical (TZ), north–south (TN) and east–west direction for a regional (left-hand panel) and a teleseismic (right-hand panel) event. A bandpass filter with centre frequency of 1 Hz is applied. Bottom trace shows the observed rotation rates around the vertical axis (RZ). Coloured vertical lines indicate arrivals of primary waves. Note the clear increase in rotational motion amplitude after the direct *P*-wave arrival in teleseismic events.

derive information about the structural heterogeneities beneath the receiver.

2 RTT FOR MODELLING SEISMOGRAM ENVELOPES

In Section 2.1 we give an introduction to the RTT in seismology. We use Monte Carlo (MC) solutions to solve the radiative transfer equations (RTEs) for the propagation of seismic energy in a heterogeneous medium with multiple anisotropic scattering in deterministic structure. The solution of the RTE using MC techniques is shortly discussed in Section 2.2. For more details on the RTT and its solutions we refer the reader for example to Przybilla & Korn (2008) or Sens-Schönfelder *et al.* (2009). In Section 2.3, we explain the modelling of multicomponent seismogram envelopes using RTT. The procedure of modelling regional and teleseismic arrivals is introduced in Section 2.4.

2.1 RTT in seismology

One suitable method to describe the propagation of seismic energy in a scattering medium is the RTT. This theory has been introduced by Chandrasekhar (1960) in the context of atmospheric sciences to describe the propagation of light through a turbulent atmosphere. RTT describes the energy flux from a radiating surface located at
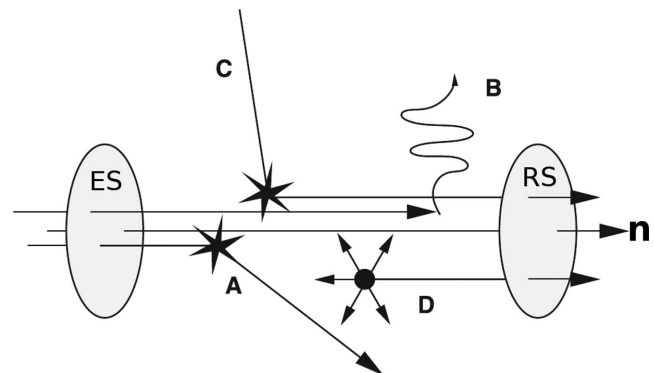

Figure 2. Conservation of energy in the RTT equations. Energy flux from an emitting surface (ES) into a receiving surface (RS) around a direction *n*. Flux reduction by scattering in other directions (A) and by dissipation (B). Flux increase by scattering from other directions into direction *n* (C) and from additional sources (D). Figure redrawn from Sens-Schönfelder *et al.* (2009).

position *r* into an unit solid angle around a certain direction *n* at time *t*. This quantity is called specific intensity *I*(*n*, *r*, *t*) and describes the angularly resolved energy flux density. Phenomenologically the transport problem can be regarded as a conservation of energy as illustrated in Fig. 2. The energy flux in an infinitesimal path element can be reduced by scattering of energy away from direction

n or by dissipation. An increase in energy flux can be achieved by scattering from other directions into direction *n* or from additional sources along the path. Since the 1960s this theory developed without rigorous connection to wave physics and was solely based on the energy balance consideration. Contributions by Weaver (1990) and Turner & Weaver (1994) helped to achieve the derivation of the RTE from the elastic wave equation for waves in a random medium (Ryzhik *et al.* 1996).

As mentioned in Section 1.1 first and simplest approaches assume single, isotropic scattering of acoustic energy, while more sophisticated models describe multiple anisotropic scattering of elastic energy. Our approach is based on the assumption of multiple anisotropic scattering of elastic seismic waves at randomly distributed small-scale heterogeneities in a deterministic macroscopic structure and is based on an algorithm detailed by Sens-Schönfelder *et al.* (2009). The algorithm is extended here to model multicomponent seismogram envelopes of rotational motions.

2.2 MC solutions to the RTE

Solutions to the RTE are often based on MC techniques. In this study we use a particle counting method, for example described by Gusev & Abubakirov (1987). The specific intensity $I(n, r, t)$ is modelled by a number density of particles $N(n, r, t)$ moving into direction *n* and located at position *r* at time *t*. The particles in the simulation are emitted from a source following a defined radiation pattern. In this study, we use an isotropic radiation pattern or an unidirectional particle emission. Particles in the simulation run are described by the following parameters.

(1) Coordinates in space and time (x, y, z, t).
(2) Particle velocity (v_x, v_y, v_z).
(3) Intensity vector $S' = (I_P, I_S)$.
(4) Polarization angle ψ.

During the course of the simulation run particles can experience multiple anisotropic scattering at medium heterogeneities following scattering patterns described in the Born approximation (Sato *et al.* 2012). This processes include mode conversion and a change of propagation direction. To account for attenuation particles lose intensity (I_P, I_S) as they propagate through the medium. When no scattering events occur, particles move according to ray theory. This includes the interaction with interfaces (reflections, transmissions and mode conversions), reflections or mode conversions at the surface or ray bending for propagation in regions with velocity gradients. To estimate the local particle density, the particles are counted in finite volumes around the receivers in consecutive time segments. Therefore snapshots of the energy density are stored in a 4-D array consisting of three spatial and one temporal dimension. Snapshots include records of *P* and *S* energy, as well as records for translational and rotational motions. To simulate the three translational and the three rotational components, projections of *I* onto specific directions (for example coordinate system axes) are used.

2.3 Modelling of multicomponent envelopes

With our algorithm we model the propagation of particles (wave packets). They represent the properties of the wavefield, if averaged over a large number. To simulate the envelopes of multicomponent seismograms, a number of transformations have to be applied that depend on the propagation direction of the particle and the polarization. These transformations allow to simulate envelopes of
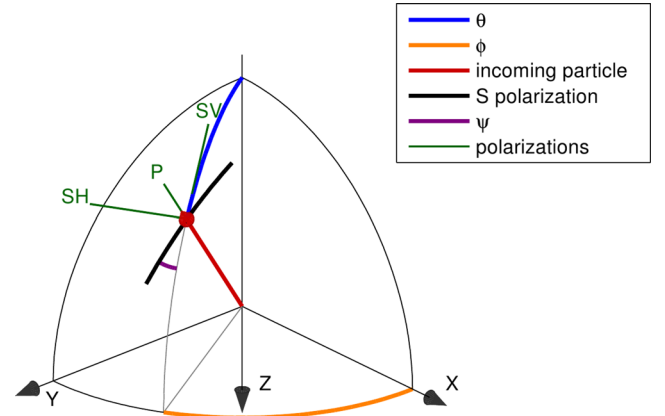

Figure 3. Illustration of relevant angles and directions. Red arrow represents the propagation direction of the particle, with θ (blue) being the particle direction measured from upwards to downwards and ϕ (orange) being the particle direction measured from north to east. Black line indicates the polarization of the *S*-particle. The polarization angle ψ (purple) is measured between the polarization direction and the vertical plane. Green lines represent the polarization directions P_P, P_{SV} and P_{SH}.

translational motions in arbitrary directions as well as rotational motions. The first step is the rotation of the Stokes vector $S' = (I_P, I_S)$ from the system with variable polarization angle ψ (see Fig. 3) into the standard system of *SV* and *SH* polarizations [$\mathbf{S} = (I_P, I_{SV}, I_{SH})$] using the following equation according to Ishimaru (1978) or Margerin *et al.* (2000):

$$\mathbf{S} = \begin{pmatrix} I_P \\ I_{SV} \\ I_{SH} \end{pmatrix} = \begin{pmatrix} 1 & 0 \\ 0 & \cos^2(\psi) \\ 0 & \sin^2(\psi) \end{pmatrix} \begin{pmatrix} I_P \\ I_S \end{pmatrix}. \tag{5}$$

The relations of intensity to the mean squared particle velocities $\langle |\dot{u}|^2 \rangle$, that is the mean squared envelopes, for the different polarizations are, according to Margerin *et al.* (2000), given as

$$\langle |\dot{u}_P|^2 \rangle = \frac{2RS}{\rho} \frac{1}{v_P} I_P \tag{6}$$

$$\langle |\dot{u}_{SV}|^2 \rangle = \frac{2RS}{\rho} \frac{1}{v_S} I_{SV} \tag{7}$$

$$\langle |\dot{u}_{SH}|^2 \rangle = \frac{2RS}{\rho} \frac{1}{v_S} I_{SH} \tag{8}$$

with ρ being the density and v_P and v_S representing *P*- and *S*-wave group velocities, respectively. *R* describes a site effect, that accounts for local density perturbations and velocity variations, *S* represents the source strength. The term $2RS/\rho$ will further be identified as *C*. Here $\dot{u}$ is assumed to be filtered in a narrow frequency band. Angle brackets indicate a time average over a few periods. The vectorial components of the velocities depend on the propagation direction of the wave packet. The propagation direction is given as $d(\theta, \phi)$, with θ being the particle direction measured from upwards to downwards and ϕ being the azimuth of the particle propagation measured from north to east, as illustrated in Fig. 3. From this propagation direction the particle polarization directions **P** for *P*, *SV* and *SH* waves are defined as:

$$\mathbf{P} = \begin{pmatrix} P_P \\ P_{SV} \\ P_{SH} \end{pmatrix} = \begin{pmatrix} \sin(\theta)\cos(\phi) & \sin(\theta)\sin(\phi) & -\cos(\theta) \\ -\cos(\theta)\cos(\phi) & -\cos(\theta)\sin(\phi) & -\sin(\theta) \\ -\sin(\phi) & \cos(\phi) & 0 \end{pmatrix}. \tag{9}$$

The direction of the coordinate system in which we record can be defined as a matrix $\mathbf{E}$ containing the unit vectors and is given by:

$$\mathbf{E} = \begin{pmatrix} E_{11} & E_{12} & E_{13} \\ E_{21} & E_{22} & E_{23} \\ E_{31} & E_{32} & E_{33} \end{pmatrix}. \tag{10}$$

This coordinate system can for example represent a standard XYZ-system, where $\mathbf{E}$ is the identity matrix (Section 2.4.2) or a ray coordinate LQT-system (Section 2.4.1). The latter system depends on the source and receiver positions and corresponds to the *P*–*SV*–*SH* axes of a direct wave illustrated in Fig. 3. The projections $\mathbf{\Pi}$ of the polarization directions $\mathbf{P}$ onto the unit vector matrix $\mathbf{E}$ are therefore defined as:

$$\mathbf{\Pi} = \mathbf{EP} = \begin{pmatrix} \Pi_{11} & \Pi_{12} & \Pi_{13} \\ \Pi_{21} & \Pi_{22} & \Pi_{23} \\ \Pi_{31} & \Pi_{32} & \Pi_{33} \end{pmatrix}. \tag{11}$$

Applying (11) to the intensity vector *S* described in (5) we obtain the mean square velocity envelopes $\langle |\dot{u}_i|^2 \rangle$ (eqs 6–8) for the different directions $i = 1, 2, 3$ of the defined coordinate system. Thus the translational motion envelopes are given as:

$$\langle |\dot{u}_1|^2 \rangle = C \left(\frac{1}{v_P} \Pi_{11}^2 I_P + \frac{1}{v_S} \Pi_{12}^2 I_{SV} + \frac{1}{v_S} \Pi_{13}^2 I_{SH} \right), \tag{12}$$

$$\langle |\dot{u}_2|^2 \rangle = C \left(\frac{1}{v_P} \Pi_{21}^2 I_P + \frac{1}{v_S} \Pi_{22}^2 I_{SV} + \frac{1}{v_S} \Pi_{23}^2 I_{SH} \right), \tag{13}$$

$$\langle |\dot{u}_3|^2 \rangle = C \left(\frac{1}{v_P} \Pi_{31}^2 I_P + \frac{1}{v_S} \Pi_{32}^2 I_{SV} + \frac{1}{v_S} \Pi_{33}^2 I_{SH} \right). \tag{14}$$

To derive envelopes of rotational motions around the coordinate system axis, we start with the general relation between the particle velocity $\dot{u}$ and the rotation rate $\dot{\Omega}$.

$$\dot{\mathbf{\Omega}} = \begin{pmatrix} \dot{\Omega}_1 \\ \dot{\Omega}_2 \\ \dot{\Omega}_3 \end{pmatrix} = \frac{1}{2} \begin{pmatrix} \partial_2 \dot{u}_3 - \partial_3 \dot{u}_2 \\ \partial_3 \dot{u}_1 - \partial_1 \dot{u}_3 \\ \partial_1 \dot{u}_2 - \partial_2 \dot{u}_1 \end{pmatrix} \tag{15}$$

For a locally plane wave with unit amplitude $|\bar{u}_0| = 1$ the wave is defined as:

$$\bar{u} = \bar{u}_0 e^{i(\omega t - \bar{k}\bar{x})}. \tag{16}$$

The partial derivatives ∂_l ($l = 1, 2, 3$) are given by

$$\partial_l \dot{u}_m = \dot{u}_{0m} e^{i(\omega t - \bar{k}\bar{x})}(-ik_l) = -ik_l \dot{u}_m, \tag{17}$$

where $m = 1, 2, 3$ and k_l is the *l*th component of the wave vector, that is the projection of the propagation direction onto the *l*th component of the recording coordinates, multiplied with ω/v_s. Here *k* is parallel to the *P*-polarization P_P. The mean square rotation rate $\langle |\dot{\Omega}|^2 \rangle$ can now be obtained from the translational motion eqs (12)–(14) using (15). As an example we show the equations for the mean squared rotation rates around the first axis of a general recording system from the intensities of *P*, *SV* and *SH* waves:

$$\langle |\dot{\Omega}_{1,P}|^2 \rangle = C \left[\frac{1}{2} \frac{\omega}{v_p} (k_2 P_{P,3} - k_3 P_{P,2}) \right]^2 \frac{1}{v_p} I_P, \tag{18}$$

$$\langle |\dot{\Omega}_{1,SV}|^2 \rangle = C \left[\frac{1}{2} \frac{\omega}{v_s} (k_2 P_{SV,3} - k_3 P_{SV,2}) \right]^2 \frac{1}{v_s} I_{SV}, \tag{19}$$

$$\langle |\dot{\Omega}_{1,SH}|^2 \rangle = C \left[\frac{1}{2} \frac{\omega}{v_s} (k_2 P_{SH,3} - k_3 P_{SH,2}) \right]^2 \frac{1}{v_s} I_{SH}. \tag{20}$$

Here we notice, that a *P* wave does not excite rotations because of its longitudinal polarization ($k \parallel P_P$). Assuming a phase relation between the *SV* and *SH* polarized waves, the total mean square rotation rate around the three axes ($i = 1, 2, 3$) can be derived from the summed contribution of the different polarizations. In this study, we are concerned with the rotation rate around the vertical axis that is only excited by horizontally polarized *SH* waves. It is given as:

$$\langle \dot{\Omega}_z^2 \rangle = \frac{1}{4} \frac{\omega^2}{v_s^3} C \left[\sin^2(\theta) I_{SH} \right]. \tag{21}$$

In the next section, we show examples for the modelling of the multicomponent translational and rotational motion seismogram envelopes in different specific coordinate systems (XYZ, LQT).

2.4 Modelling of regional and teleseismic events

In the following sections we describe the modelling approaches to simulate multicomponent envelopes for shallow regional events (Section 2.4.1), as well as for teleseismic *P*-wave arrivals (Section 2.4.2).

2.4.1 Simulation of regional events

For the simulation of shallow regional events the translational and rotational seismogram envelopes are modelled in a ray based co-ordinate system (LQT-system). The choice of the LQT recording system is convenient as it can exploit the cylindrical symmetry of the problem. It allows to stack data from stations at different azimuth but similar distance, thus saving computational time in the MC-RTT simulations due to the computation of stacked envelopes. The recording system is dependent on the position of the source as well as on the location of the receiver element in the medium. The L-component therefore represents the direct path from source to receiver, the Q-component represents the direction perpendicular to the radial component in the vertical plane and the T-component is perpendicular to the L and Q directions. The unit vector matrix $\mathbf{E}_{\text{LQT}}$ for the LQT-coordinate system according to equation 10 is therefore identical to the matrix describing the *P*, *SV* and *SH* polarizations (eq. 9). In the simulation we model an isotropic, point source with a fixed *P* to *S* energy ratio [see for example Sato *et al.* (2012) or Shearer (1999)] of ~0.05. To illustrate the energy propagation, we simulate cross-sections through the seismic wavefield in the vertical plane for different depths. An example of the simulation output is shown in Fig. 4. The simulations of regional events with a hypocentre in the crust show strong reverberation of seismic energy in the crust. A striking feature is the formation of guided *S* waves. It is clearly visible, that the seismic coda following the direct *S*-wave arrival is mainly composed of scattered *S* energy, which is homogeneously distributed in space. Scattered *P* energy only plays a minor role in the generation of the seismic coda after the *S*-wave arrival.

2.4.2 Simulation of teleseismic events

To compute seismogram envelopes for teleseismic arrivals, we do not model the full path from the distant source to the receiver, but rather model the excitation by a plane, incoming wave front. In the realistic setup this wave front can be seen as a multitude of directed, parallel incoming particles and is illustrated for the vertical and tilted incidence in Figs 5(a) and (c). The green lines in Figs 5(a) and (c) indicate the plane wave fronts. In the simulations such a wave can
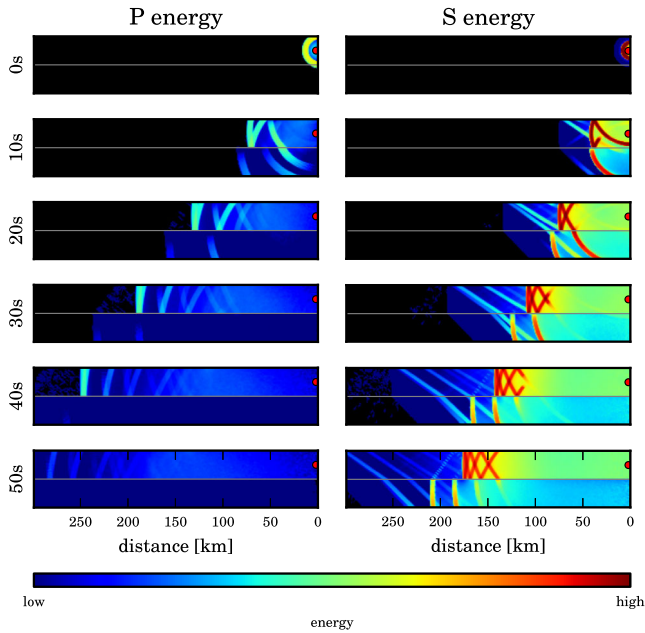
P energy   S energy

Figure 4. Energy propagation from a regional, shallow earthquake. An isotropic source (red circle) with a fixed *P* to *S* energy ratio is placed in the strongly scattering crust overlaying the transparent mantle (no scattering in the lithospheric mantle). Slices show snapshots of *P* energy (left-hand column) and *S* energy (right-hand column) for different times. Time is measured in seconds after the first arrival of energy at the surface. The development of guided *S*-energy (Lg-waves) is clearly visible. To increase the contrast for illustration purposes the ratio of emitted *P*- and *S*-energy at the source is set to 0.2.

be excited by many different unidirectional particle sources that fire with an offset dependent time delay if the incident angle is oblique. This time delay is indicated by the blueish triangles (positive time delay) and the reddish triangles (negative time delay) in Fig. 5(d). The resulting seismogram at one specific receiver in the realistic setup is the sum of the traces generated by all individual single directed sources measured at the receiver. In contrast to this natural setup with multiple sources, the model setup in our simulations makes use of the translational symmetry of the setup and only consists of one directional source. The seismogram for one receiver (central receiver in the model setup, Figs 5b and d) is then given as the integral over all seismograms recorded at the surface receivers. Due to the translational invariance, the path from each directed source to the receiver can also be found in the model setup (see Fig. 5). Identical travel paths are indicated by same colours. The simulations for teleseismic arrivals are carried out in a standard cartesian XYZ-coordinate system. An example of the simulation output for a vertically incident teleseismic *P* wave is shown in Fig. 6. In this simulation we use a vertically upwards directed, purely compressional single source in a homogeneous mantle. Even though initially the energy propagates only vertically, the development of horizontally propagating *P*- and *S*-energy wave trains is clearly visible after a short duration. This can be explained solely with scattering of seismic energy in the crustal part of the lithosphere. Similar to the excitation by a crustal source (Fig. 4) the seismic energy propagates as guided *S* wave even though the source is a pure *P* source. To infer a seismogram envelope from Fig. 6 that shows the energy distribution in the model setup one needs to integrate over the surface of each time slice. This integration is required to transform from a model with one source and multiple receivers (Figs 5b and d) to the natural setup with a plane wave front represented by multiple

sources and one single receiver (Figs 5a and c). An example of the resulting seismogram envelopes is shown in Fig. 11.

3 STUDY AREA AND DATA

The region of interest in this study is in the southeastern part of Germany close to the borders of the Czech Republic and Austria. An overview of the study area with the station distribution and the earthquakes used for the local inversion is shown in Fig. 7. Stations of the Gräfenberg array (GR) are part of the Seismological Central Observatory (SZO) operated by the Federal Institute for Geosciences and Resources (BGR). The five stations UBBA, MOX, BRG, TANN and WET are part of the German Regional Seismic Network (GRSN). The stations of the Gräfenberg array are deployed at remote sites on a plateau of the Frankonian Jura. This formation is made of comparatively homogeneous Upper Jurassic Limestone and is overlain by a sedimentary wedge of varying thicknesses between 400 and 1150 m (Krüger 1994). The lithospheric basement of this formation belongs to the Variscian Belt (Franke 1989). A crustal thickness of about 30 km is estimated by Zeis *et al.* (1990) for the Gräfenberg area with a total lithospheric thickness between 80 and 100 km (Mueller & Panza 1986). The ringlaser instrument (WET) is directly deployed on bedrock Gneisses (Klügel *et al.* 2001).

4 INVERSION OF REGIONAL EARTHQUAKE ENVELOPES FOR SCATTERING PARAMETERS

In this application, the envelopes of regional swarm-earthquakes in the Vogtland area (Fig. 7) are inverted for scattering and attenuation parameters of the random medium representing the local crustal material. The source area is selected because of its proximity to the ring laser in Wettzell. The swarm activity in the Vogtland area generates multiple earthquakes of moderate size that are used to create averaged reference seismogram envelopes. We use reference seismogram envelopes for different epicentral distances and perform the forward modelling as described in Section 2.4.1. The genetic inversion algorithm that estimates the best fitting parameters is detailed in Section 4.1. Section 4.2 gives details about the inversion setup, the results of the inversion of regional earthquakes are then presented in Section 4.3.

4.1 Genetic inversion approach

In the inversion process we use a genetic approach, for example described by Mitchell (1996). We assume an exponential autocorrelation function to describe velocity and density fluctuations in the random medium. In principal there are eight free parameters in the inversion: fluctuation strength ϵ, correlation length a, the intrinsic quality factor Q_i^S for *S* waves and Q_i^P for *P* waves in the crust, and in the mantle respectively. In the actual inversion we restrict the parameter space. In the beginning of the inversion mantle parameters are fixed to reasonable values taken from Sens-Schönfelder *et al.* (2009). As synthetic tests indicate, changes in the mantle properties do not show significant influence on the simulation results at this distance range. Additionally, we do not invert for Q_i^P and Q_i^S independently, but rather invert for Q_i^S with a fixed Q_i^P / Q_i^S ratio (Shearer 1999). This leaves us with three free parameters in the crustal part of the medium: $\epsilon_{\rm crust}$, $a_{\rm crust}$ and $Q_{i,\rm crust}^S$. Starting values for the free parameters are set to reasonable values obtained from the literature and a first population of starting models is generated
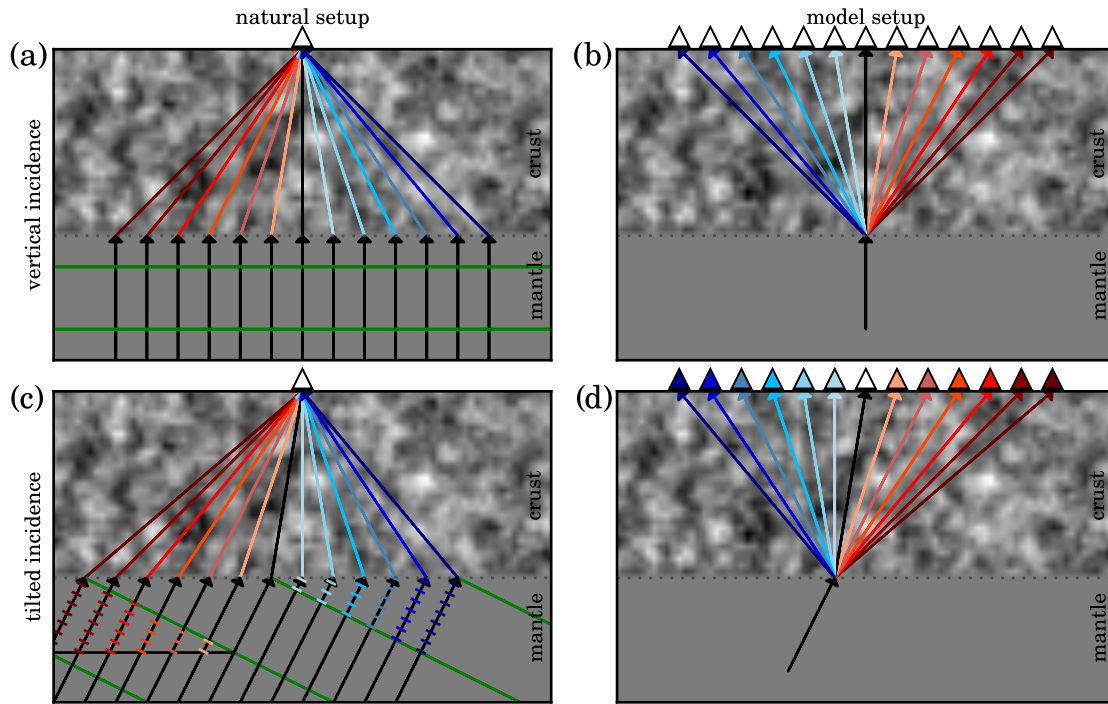
Figure 5. Modelling of a plane wave front with a strongly scattering crust overlaying a transparent mantle. Left-hand column illustrates a plane wave front (green) in the realistic setup for vertical (a) and tilted incidence (c). The plane wave can be seen as a multitude of parallel incoming particles. In the model setup (b) and (d), the plane wave is modelled by one single incoming wave segment, its energy is recorded along the whole surface. Arrow colours in the left- and right-hand column indicate identical travel paths. For the tilted case of the model setup a time correction has to be applied for receivers apart from the central receiver. This time correction is indicated by colours inside the receivers in the tilted model setup. Blueish triangles indicate a positive time delay, reddish triangles indicate a negative delay.
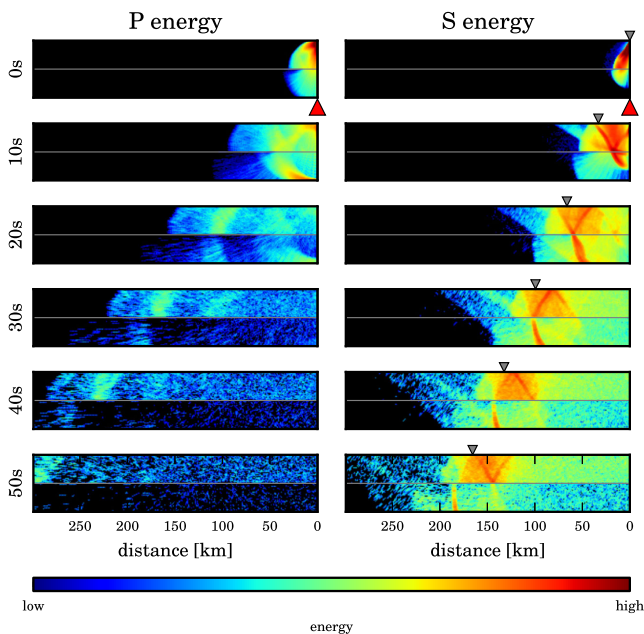

Figure 6. Energy propagation for a teleseismic event. A vertically directed purely compressional source (red arrow) is placed in the transparent mantle, underlying a strongly scattering crust. Slices show snapshots of *P* energy (left-hand column) and *S* energy (right-hand column) for different times. Time is measured in seconds after the first arrival of energy at the surface. Even though the energy is emitted only vertically from the source, the emergence of guided *S*-wave energy is clearly visible.

by random alteration of the starting values within a certain range. For these models we calculate the forward simulations using MC techniques and compare them to so called reference envelopes that are generated from the seismic data. Misfits M between the simulated envelopes S and the reference envelopes R obtained from stacked earthquakes are calculated as the logarithmic L1-norm:

$$M = \sum_{i=0}^{n} \sum_{j=0}^{m} |\log(R[i, j]) - \log(S[i, j])| \qquad (22)$$

with n being the number of traces depending on the number of stations and on the number of recorded components. m is the number of samples in each trace. Using logarithmic differences ensures that high-amplitude direct waves and lower-amplitude coda values, have a similar weight in the misfit calculation. Furthermore the misfit calculation using the L1-norm is less sensitive to fluctuations in the forward simulations or the reference traces. In each iteration cycle a new model population is generated by recombination and mutation of the fittest models (models with small misfit values) and by creation of some completely new models. Random models are created throughout the entire inversion process to enforce sampling of the whole model parameter space. Mutation alters selected parameters of good models and ensures the creation of new models in the vicinity of minima in the misfit function. Recombination leads to a dense sampling of the model space especially in the vicinity of fit models. The inversion setup is explained in Section 4.2.

4.2 Inversion setup

Forward models are calculated using MC solutions to the RTE following the method described in Section 2.4.1. To simulate
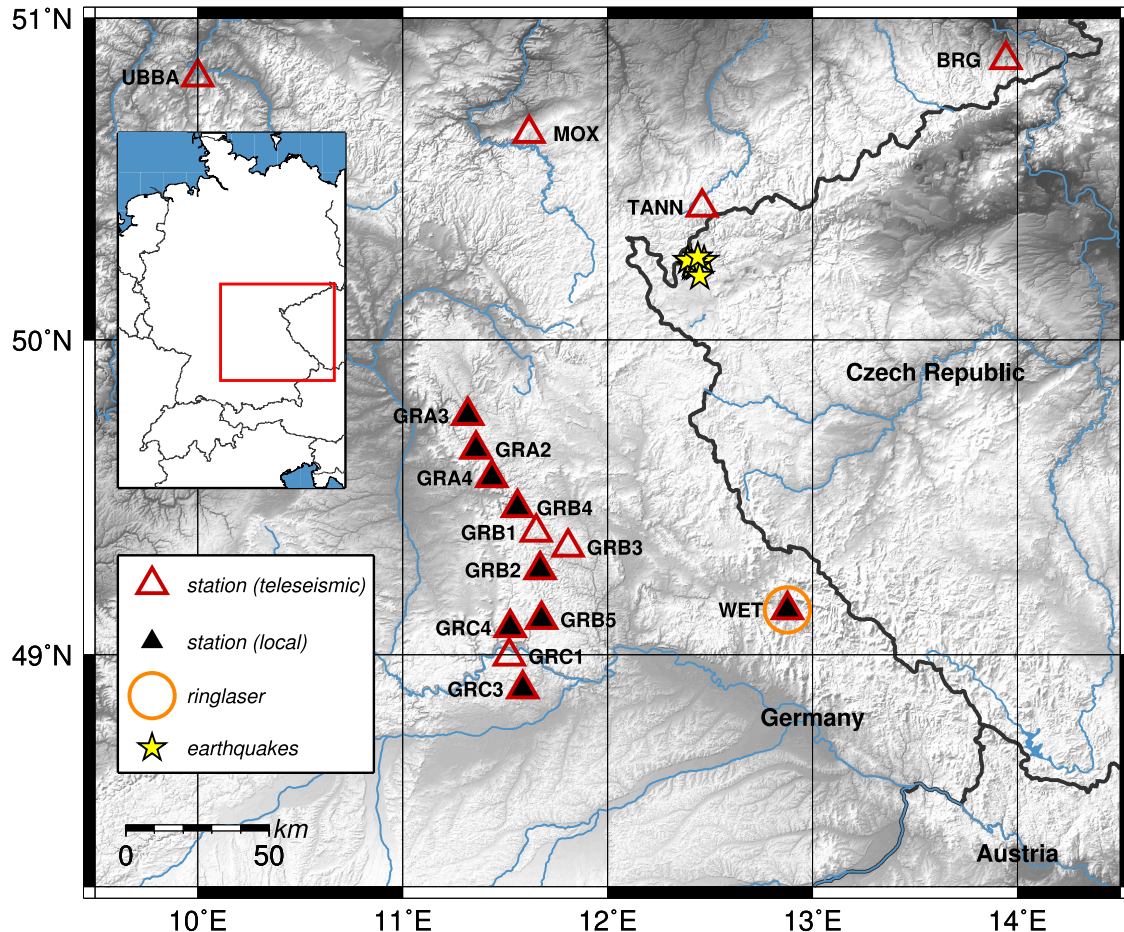
Figure 7. Map of the study area. Empty red triangles indicate stations used for the study of the teleseismic arrivals (see Section 5). Solid black triangles represent receiver used in the regional case (see Section 4) with the investigated local earthquakes in the Vogtland region (yellow stars). The ringlaser located at the Fundamentalstation in Wettzell is indicated by the orange circle. Grey shading indicates topography.

translational LQT snapshots of the wavefield we record the seismic energy in the LQT-system in a domain with lateral size of 400×400 km. We note, that there are no boundary effects in the simulations, as the particle propagation is modelled throughout the full time interval irrespective of the particle location. In the vertical direction we model a 30-km-thick crust overlaying a half-space representing the mantle. The source is placed in the centre of the model at a depth of 5.5 km, which is the mean depth of the swarm-earthquakes used here. This setup allows to compute azimuthally stacked cross sections in the distance range from 0 to 200 km. As source we chose an isotropic radiation pattern. The energy ratio between radiated *P* and *S* energy is fixed at ~0.05 (Shearer & Earle 2008). Parameters in the mantle are fixed to fluctuation strength $\epsilon = 0.5$ per cent, correlation length $a = 2$ km and $Q_i^S = 143$ ($Q_i^P = 321$) according to Sens-Schönfelder *et al.* (2009). As crustal starting values we chose $\epsilon = 0.5$ per cent, $a = 2$ km and $Q_i^S = 600$ ($Q_i^P = 1350$) (Dziewonski & Anderson 1981; Sens-Schönfelder *et al.* 2009). We invert for Q_i^S with a fixed Q_i^P to Q_i^S ratio of 2.25 (Shearer 1999). Reference seismogram envelopes are calculated using swarm-earthquakes in the Vogtland-area (Fig. 7, Table 2) recorded at multiple stations of the Gräfenberg array (GR) and station WET. (Fig. 7, Table 3). Station WET is included in the inversion process, as in Section 5.2 we will use the vertical rotation observed at that station. The computation of the reference seismogram envelopes involves processing of individual records, the estimation of correction factors for site amplification and event

Table 2. Swarm-earthquakes used in the inversion.

Region	UTC-time	Mag	Lon (°)	Lat (°)	*d* (km)
Vogtland	2011-08-28-06-45-08	3.0	12.47	50.25	4
Vogtland	2011-08-26-15-27-24	3.1	12.41	50.24	6
Vogtland	2011-08-26-06-54-05	3.6	12.42	50.23	5
Vogtland	2011-08-26-06-15-45	3.3	12.41	50.23	6
Vogtland	2011-08-26-00-35-02	3.2	12.43	50.23	4
Vogtland	2011-08-26-00-15-34	3.4	12.39	50.25	5
Vogtland	2011-08-25-23-33-21	4.0	12.45	50.20	9
Vogtland	2011-08-25-23-05-41	3.6	12.44	50.26	5

size and finally the stacking of records from different events. For the processing of individual records the following steps are performed.

(1) Demeaning of the traces.
(2) Instrument response removal.
(3) Bandpass filtering (4–8 Hz).
(4) Distance correction (stretching).
(5) Subtraction of noise level.
(6) Rotation from ZNE into the LQT system.
(7) Calculation of Hilbert envelopes.
(8) Smoothing of the envelopes.

The correction of the instrument response is done to enable broad-band comparison of absolute amplitudes of translational and rotational measurements. A distance corrections for each

Table 3. Stations used in the inversion.

Network	Station	Lon (°)	Lat (°)	Equipment
GR	GRA3	11.32	49.76	STS-2
GR	GRA2	11.36	49.66	STS-2
GR	GRA4	11.44	49.57	STS-2
GR	GRB4	11.56	49.47	STS-2
GR	GRB2	11.67	49.27	STS-2
GR	WET	12.88	49.14	STS-2
GR	GRB5	11.67	49.11	STS-2
GR	GRC4	11.53	49.09	STS-2
GR	GRC3	11.59	49.89	STS-2

station–earthquake pair is necessary as we stack different earthquakes with slightly variable epicentral distances (less than 5 per cent) to obtain smooth reference seismogram envelopes. The stretching aligns phases of equal slowness $[t' = t(1 + (r_0 - r)/r]$, with t is the lapse time, t' is the corrected lapse time, r is the epicentral distance, r_0 is the average epicentral distance of events used for stacking). After these processing steps site amplification factors for the stations and source energies for the events are computed with the coda normalization method [CNM, Aki (1980)] to correct the envelopes. This ensures that even though magnitudes of the events are different they get similar weight in the stacking and maintain consistent relative amplitudes in different epicentral distances. After these correction the seismogram envelopes are stacked to obtain the reference envelopes for the inversion.

4.3 Results of the inversion

In this section the results of the inversion for crustal scattering and attenuation parameters from regional swarm-earthquakes are presented. During the inversion process more than 2000 simulations for different sets of parameters were calculated and compared to the reference envelopes. The simulations cover a model space of roughly $0.1 < \epsilon < 20$ per cent, $100 < Q_i^S < 5000$ and 10 m $< a < 10\,000$ m. The resulting misfit values for the different pairs of parameters $(a - \epsilon, Q_i^S - \epsilon, Q_i^S - a)$ are shown in Fig. 8. The best model, that is the model with the lowest misfit has following crustal scattering and attenuation parameters for a medium with an exponential autocorrelation function: fluctuation strength $\epsilon = 2.9$ per cent, correlation length $a = 270$ m and intrinsic S-wave quality factor Q_i^S 667 ($Q_i^P = 1500$). In Fig. 8, we observe a number of simulations located around the best simulation with a misfit value that is not

significantly different from the minimum. Especially in the parts of the coda of the direct P and S waves some weak fluctuations can be observed in the simulations. Due to these statistical variations the resulting misfit for simulations with identical parameters can differ by ~1.5 per cent. This uncertainty is calculated by comparing multiple simulations using identical medium parameters. Even if all the simulations are computed with the same set of medium parameters, we end up with small differences between them. This differences are a measure of the uncertainties of our simulations. If we take into account these uncertainties of the misfit values, parameters, that can explain the data equally well, are in the range $2.5 < \epsilon < 3.5$ per cent, 100 m $< a < 400$ m and $580 < Q_i^S < 750$ (see Fig. 8, green ellipses). In Fig. 9, we show the comparison of the best model with the reference seismogram envelopes. Here we do not show all stations used in the inversion process (Fig. 7, Table 3), but restrict the plot to four stations at different distances (GRA2, GRB4, WET and GRC4). Station WET is highlighted in orange as it will further be used for modelling of teleseismic arrivals including rotational motions (Section 5). Some differences can be noticed between the simulations and the reference envelopes, especially for the direct P- and S-wave arrivals and the P coda. These differences can be explained to a large extent by the isotropic source radiation used in our modelling or by a Q_i^P/Q_i^S ratio that is different from the theoretical value assumed here. An influence of the radiation pattern is plausible because we average over different earthquakes while constructing the reference envelopes, but apparently the similarity of the source processes (Fischer *et al.* 2013) hinders an efficient averaging of the radiation pattern during stacking. In contrast the coda of the S wave can be modelled well. Our suggested crustal scattering and attenuation parameters are in good agreement with the results of other studies for non-volcanic areas. Especially the comparison to studies by Sens-Schönfelder & Wegler (2006), Sens-Schönfelder *et al.* (2009), Calvet & Margerin (2013) and Rothert (2000) is of interest, as they investigate scattering and attenuation parameters in similar regions. For a comparison of the estimated attenuation and scattering parameters see Table 1 and Section 1.2.

5 SIMULATION OF TELESEISMIC RECORDS OF *P*-CODA ENVELOPES

In the previous section crustal scattering and attenuation parameters were estimated using an established technique of inverting translational motions from regional, shallow swarm-earthquakes.
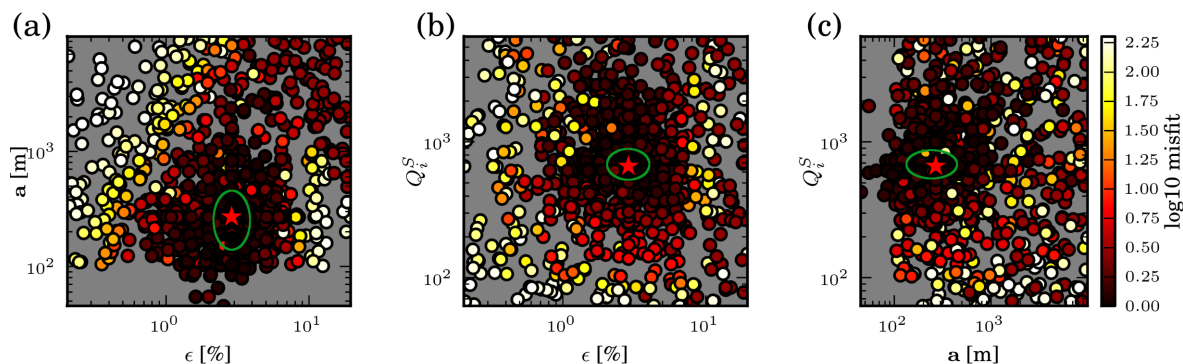

Figure 8. Misfit values for different pairs of free parameters in the inversion process. (a) Correlation length a against fluctuation strength ϵ. (b) Intrinsic quality factor Q_i^S against fluctuation strength ϵ. (c) Intrinsic quality factor Q_i^S against correlation length a. Darker colours of the symbols indicate a low misfit value (good model), brighter colours represent a (bad) model with a high misfit value. Misfits are illustrated in a logarithmic scale to increase the contrast for visualization. Misfits are scaled to the simulation with the lowest misfit value (red star). Note the clear area of simulations with low misfit values around the best model. Green ellipses indicates models with misfit similar to the best model (difference ~1.5 per cent).
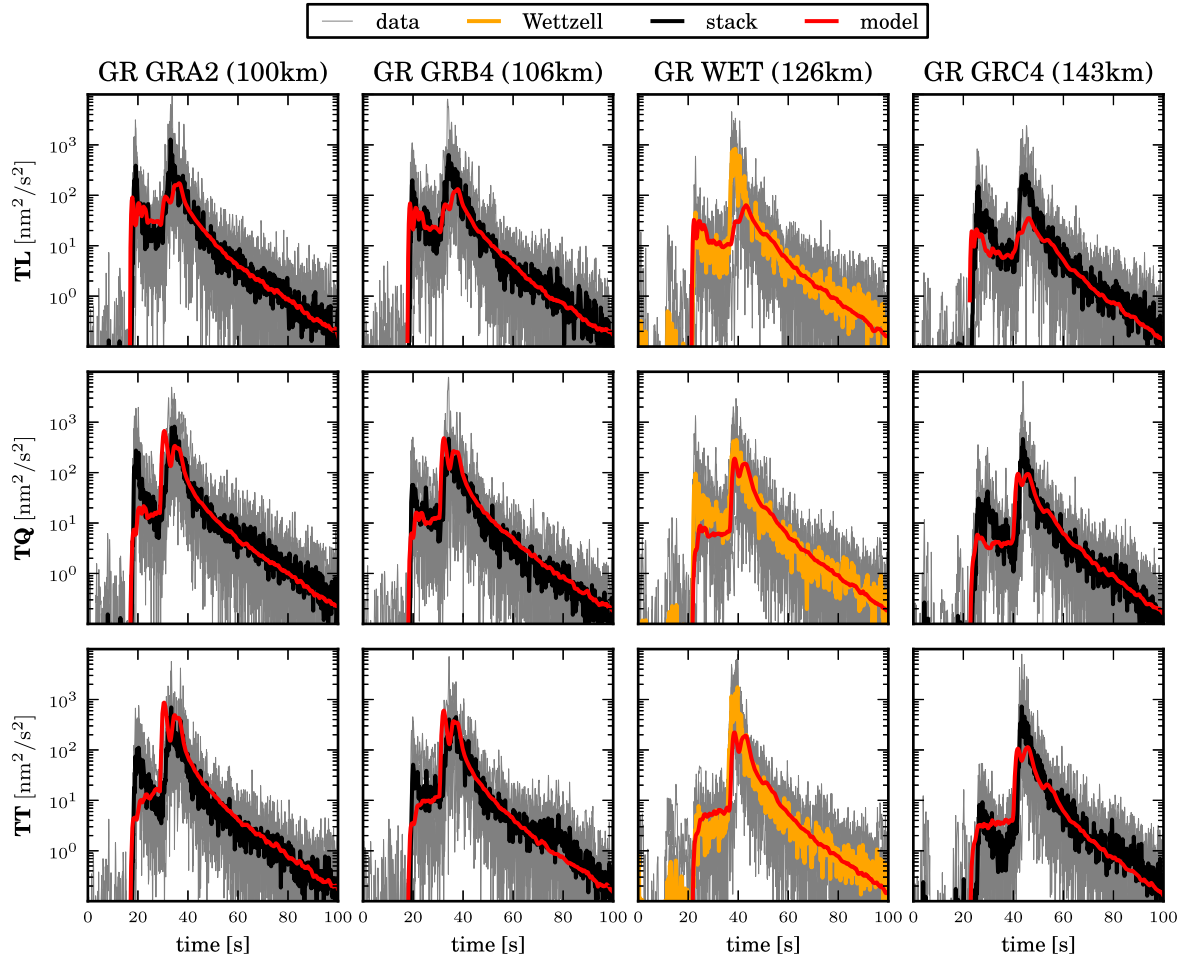
Figure 9. Comparison of reference seismogram envelopes from the local swarm earthquakes and simulated envelopes for the best model. Simulations are shown in red, reference traces are shown in black or orange in the case of WET. This station will further be used for the modelling and comparison of rotational envelopes from teleseismic events. Columns represent different stations with different epicentral distances (see round brackets) increasing from left-to right-hand side, rows show the different components in the ray LQT-coordinate system. Grey lines indicate traces for the individual earthquakes. Units are given in nm^2 s^{-2} (intensity) and scaled to the coda average at around 80 s. In this figure only four of the nine stations used in the inversion process are shown.

This estimated set of parameters is now used to model translational and rotational motion seismogram envelopes for teleseismic arrivals. The computed envelopes are compared to translational and rotational motion records from deep teleseismic events. We will focus our attention to the station WET, located at the Fundamentalstation in Wettzell, as this station offers recordings of the three translational motions as well as measurements of the rotation rate around the vertical axis performed by a ringlaser. In Section 5.1, we investigate the performance of the ringlaser in comparison to the colocated intertial seismometer. Section 5.2 shows the comparison of the simulation results with envelopes of teleseismic *P* coda.

5.1 Ringlaser response

The optical measurement principle of the ringlaser results in a flat frequency response. The data, however are the product of the instrument and the data acquisition system. To investigate the frequency response of the rotational motion sensor, we compare the PSD of the rotation data to the PSDs of the three translational components. This comparison is shown in Fig. 10. The PSD functions are calculated using data from the *S*-wave coda of a regional event. To compare the PSDs of translational and rotational motions, the amplitudes of the PSDs have to be scaled. PSDs of the ground velocity are multiplied

by the angular frequency to obtain the acceleration spectrum and rotation rate data are scaled with two times the local *S*-wave phase velocity prior the computation of the PSD. For plane horizontally polarized shear waves the accelerations and scaled vertical rotation rates should have similar amplitudes (see eqs 15 and 17). We can observe relatively stable PSDs for the translational components over the entire frequency range (see Fig. 10), representing the source spectrum of the event. On the other hand we notice a clear drop in the PSD of the rotational components for frequencies above 1 Hz. This sudden drop in the PSD is explained by limitations of the data acquisition system of the ringlaser data. For that reason, we use the frequency band below 1 Hz for the comparison of rotational and translational motion envelopes from the station WET.

5.2 Modelling of teleseismic *P* coda

In this section, we compare translational and rotational motion envelopes from teleseismic *P* coda with simulations based on the inversion results from the regional events and the method described in Section 2.4.2. We use four deep teleseismic events in the distance range between 70.8° and 73.3° (Table 4). The deep events in these distances have the advantage, that the crustal structure beneath the receivers is excited by an almost plane wave. As we
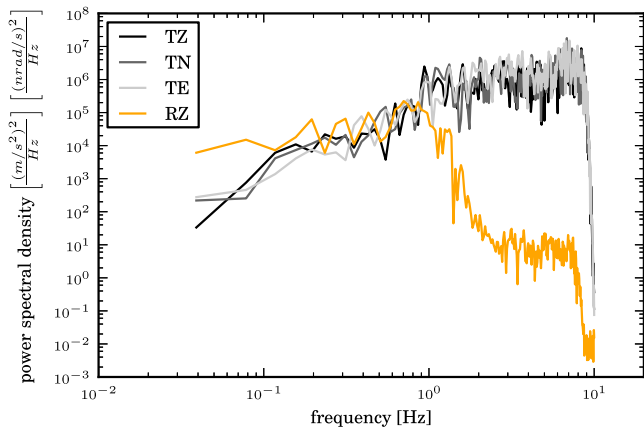
Figure 10. Power spectral density of the three translational motion components and the rotation around the vertical axis (RZ) for the *S*-wave coda of a regional event. Translational components are shown in grey colours, the rotational component is shown in orange. We notice a clear drop in the PSD for the rotational component at around 1 Hz, whereas the translational component PSDs are stable over the entire frequency range. TZ indicates motion in the vertical direction, TN in north–south direction and TE indicates motion in the east–west axis.

exclude the depth phase *pP* that is scattered in the crust at the source side we can assume that interaction of the waves with structure is weak on the way from the source to the model domain beneath the receiver. Thus the signal that enters the model is the source time function of the earthquake. In the selected epicentre distances the first arriving phases are *P* and *PcP*, which have similar traveltimes (617–648 s) and also show a similar incidence angle at the receiver of $14°–18°$. Traveltimes and incident angles for *P* and *PcP* waves are calculated using the iasp91 model introduced by Kennett & Engdahl (1991). To synthesize the seismogram envelopes we use the model introduced in Section 4 consisting of a heterogeneous layer with 30 km thickness representing the crust over a transparent half-space representing the mantle. Transparent indicates, that no scattering of seismic energy occurs. The scattering and attenuation parameters are chosen according to the results found in Section 4. We use a fluctuation strength of 2.9 per cent, a correlation length of 270 m and an intrinsic quality factor Q_i^S of 667 ($Q_i^P = 1500$) to describe the crustal part of the model. The source is placed below the crust inside the transparent mantle and only radiates energy into the direction of the incident plane wave. The arrival of *P* and *PcP* energy is simulated in two steps. First, we simulate the arrival of *P* energy with the corresponding theoretical incidence angle. In a second step the arrival of *PcP* is simulated using the incidence angle for *PcP* energy and taking into account the reflection coefficient for reflected *P* energy at the core-mantle boundary. In the algorithm we model a source, in which all energy is emitted at the same time. The resulting envelopes for *P* and *PcP* arrivals are then convolved with the mean square envelope of the source time function of the earthquake. Source time functions are extracted from

the SCARDEC method described in Vallée *et al.* (2011) and Vallée (2013). Envelopes of *PcP* energy are shifted according to the difference in *PcP* and *P* traveltime (Table 4). The resulting traces are added to obtain the envelope representing *P* and *PcP* energy. A comparison between the simulated arrivals and the recordings for the three translational motions and the rotation rate around the vertical axis are shown in Fig. 11. The figure shows the envelopes recorded at all the stations (Fig. 7) as grey lines and their average in black. Station WET is highlighted in orange as it corresponds to the envelopes of the rotation rate. Modelled translational (top three rows) and vertical rotational (bottom row) envelopes are plotted in red. To compare simulations and data, the envelopes are scaled to the average coda amplitude in a late time window. Note that we only use the average coda amplitude in a late time window of the total translational envelope to scale all three translational envelopes as well as the vertical rotational envelopes with a single scaling factor. This is possible due to the assumption of plane wave propagation and the corresponding scaling described in eqs (15) and (17). The first thing to note in Fig. 11 is the complexity in the data. The different durations of the direct *P* pulse is well accounted for by convolution with the source time function plotted in green in Fig. 11. The coda decay of the translational motion envelopes is fairly well modelled for all events. The rotation rate envelopes show much larger fluctuations as the translational reference envelopes for two reasons. First, no averaging over different stations could be performed as there is only one instrument of this type available. Secondly, the noise level of the ringlaser is high compared to the noise level of classical seismometers. So the main characteristics of the rotation data are the absence of a direct pulse at the arrival time of the *P* wave and a decay similar to the translational envelopes. As shown in the bottom row of Fig. 11 these main characteristics of the data are modelled well by the synthetic envelopes.

6 DISCUSSION

We use an inversion of regional three-component seismogram envelopes at different epicentral distances to infer parameters of the crustal heterogeneities in southeast Germany. The resulting values $2.5 < \epsilon < 3.5$ per cent, $100\,m < a < 400\,m$ and $580 < Q_i^S < 750$ for the fluctuation strength, the correlation length and the *S*-wave quality factor are in fair agreement with comparable studies in Europe. Sens-Schönfelder & Wegler (2006) revealed an intrinsic quality factor Q_i^S of 769 in Germany. Another study by Sens-Schönfelder *et al.* (2009) in the Pyrenees (France) describes the attenuation of *S* waves with a value Q_i^S of 625. Calvet & Margerin (2013) confirmed these results in France, where they found $Q_S \sim 769$. The correlation length of the exponential type fluctuations of $a = 250\,m$ together with a fluctuation strength $\epsilon = 2.9$ per cent obtained in the present study leads to a transport mean free path of *S* waves of $l^* = 420\,km$ at 6 Hz. This value is supported by Calvet & Margerin (2013) who found $l^* \sim 400\,km$ for their preferred model at 6 Hz (Table 1). Sens-Schönfelder *et al.* (2009) estimated a transport

Table 4. Deep teleseismic events used for the comparison, with M_w being moment magnitude, Δ the epicentral distance from station WET. $t_{PcP} - t_P$ is the arrival time of the *PcP* wave after the *P*-wave onset time.

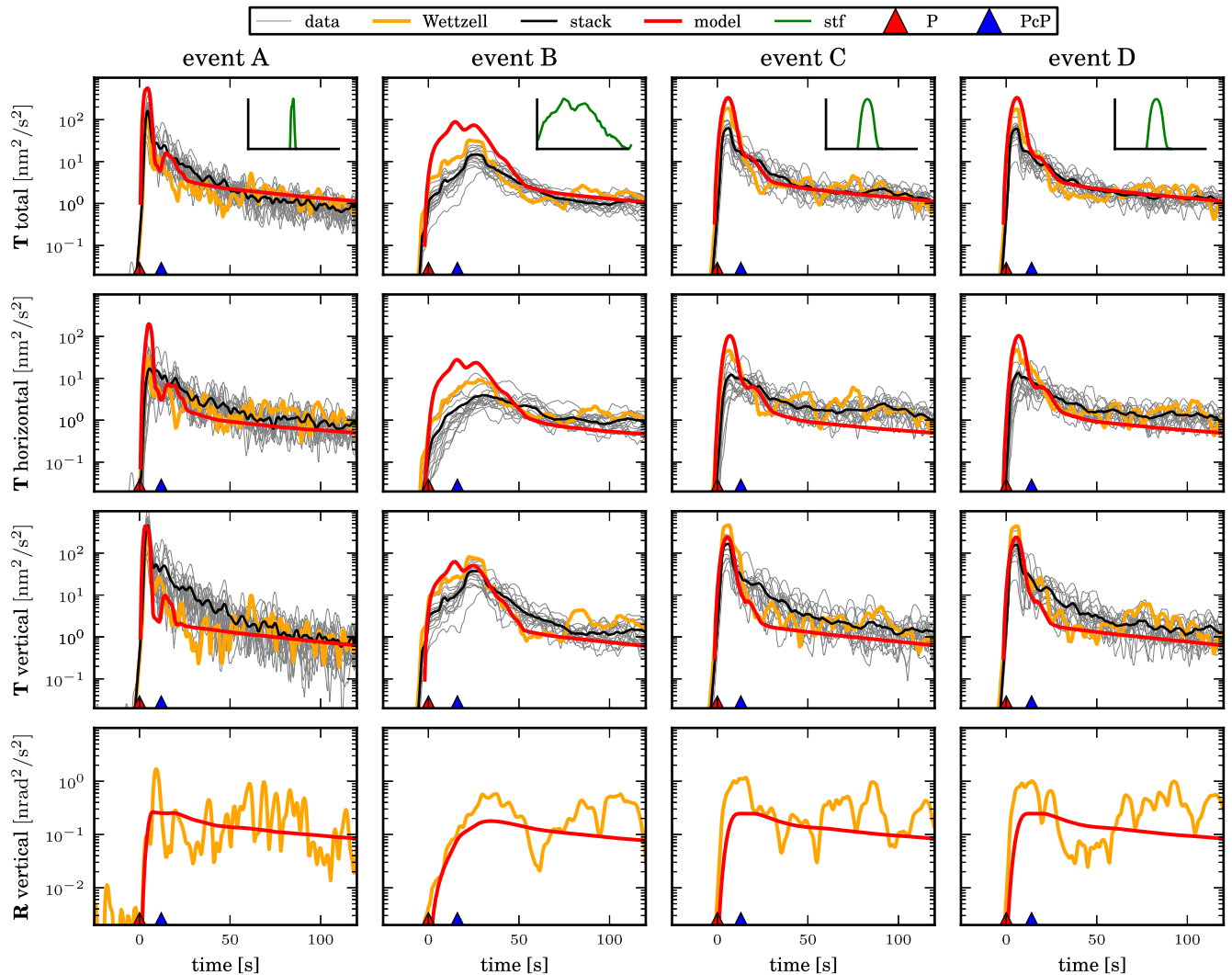| Event id	Region	M_w	Δ (°)	Depth (km)	Origin time UTC	$t_{PcP} - t_P$ (s)
Event A	E-Russia,NE-China	6.3	73.3	549	2013-04-05-13:00:01	12
Event B	Sea of Okhotsk	8.3	70.8	605	2013-05-24-05:44:48	16
Event C	Sea of Okhotsk	6.7	72.7	629	2013-05-24-14:56:31	13
Event D	Sea of Okhotsk	6.7	72.2	573	2013-10-01-03:38:22	14

Figure 11. Comparison of simulations and data for teleseismic arrivals. Results of the simulations are shown in red, black lines represent a stack of all available stations (see Fig. 7). The grey lines in the background represent traces for each single station. The station WET is highlighted in orange colour. Top row shows total translations, the second row gives the horizontal translations and the vertical translation is shown in the third row. Columns represent the different earthquakes given in Table 4. Rotational motions around the vertical axis are shown in the bottom row. As only for station WET rotational motion records are available, we can only compare one recorded trace to the simulations. Source time functions used for the convolution with the simulated traces are indicated in green in the same time scale as the data. The time scale is chosen such that *P*-wave arrival is a time zero. Units are given in nm^2 s^{-2} or nrad^2 s^{-2} (intensity) and scaled to a coda average. Theoretical arrivals of *P*- and *PcP*-energy are marked with red and blue triangles, respectively.

mean free path of 761 km at 3 Hz which is also comparable to our results. Rothert ([2000](#)) inferred similar correlation lengths *a* and fluctuations of velocity in the crust from the analysis of teleseismic events at the Gräfenberg array. The agreement with results of Calvet & Margerin ([2013](#)) is remarkable as these authors inverted the lapse time dependence of coda-*Q* with a model of multiple anisotropic acoustic scattering in an infinite half space. In contrast our model features elastic scattering in a layer-over-half-space structure. This correspondence confirms the importance of *S*-wave scattering in the crust, but the more realistic modelling in our approach allows to simulate full seismogram envelopes including *P*-wave energy and the early coda. Comparison of the envelopes in Fig. 9, however, indicates that detailed modelling of the early coda requires the incorporation of the source radiation pattern even in the present case where an averaging is performed over different events.

The separation of the modelling domain into a scattering crust and a transparent mantle allows to model the excitation by sources

outside the scattering medium. This possibility is used for modelling the envelopes of teleseismic *P*-coda including rotational motions. Using the parameters from the inversion of the regional seismogram envelopes we modelled the first 100 s of teleseismic *P*-wave coda. This time window includes the direct *P* phase, the *PcP* phase and the beginning of the coda. Our observations are restricted to this time interval to exclude the depth phase pP which arrives ~120 s after the direct *P* wave for this distance and depth range. The reason for excluding pP is its dependence on the structure on the source side of the path. As pP penetrates the crust on the source side twice its shape is not only influenced by the source–time function of the event but also by the heterogeneity of the crust above the source. We observed significantly different shapes of pP envelopes for events of comparable size and depth in different source regions. Also combining *P* and pP observations introduces a dependency on the radiation pattern of the event that influences their relative amplitudes. Our modelling results show reasonable agreement with the
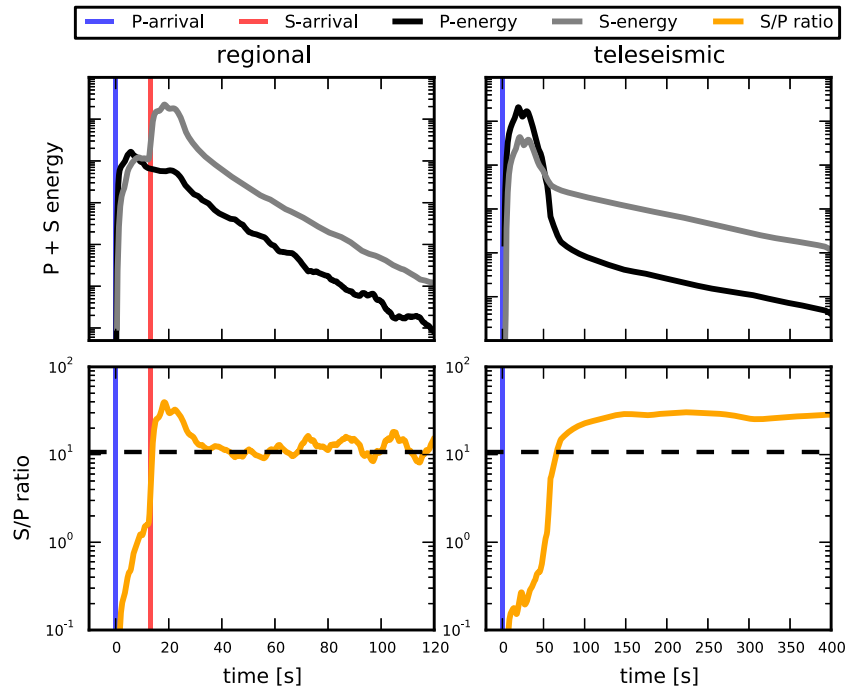
Figure 12. Temporal evolution of the equipartition ratio for *S*- and *P*-energy. Top row shows *P*- and *S*-energy for a regional simulation at en epicentral distance of 100 km (left-hand side, compare Fig. 9) and for the teleseismic case (right-hand side, compare Fig. 11). Bottom row gives the ratio of *S* and *P* energy. Dashed black line represents the theoretical equipartition value of 10.7 for our model.

observed seismogram envelopes for translational motion as well as for vertical rotational motion (Fig. 11). We focus on comparing the peak of the direct arrival and the decay of the coda for the vertical rotation rate and the translational envelopes. An additional observable is the relative amplitude of the translational and rotational data. The different width of the direct *P*-pulse is well accounted for by convolution with the source time function plotted in green in Fig. 11. Also the coda decay of the translational motion envelopes is fairly well modelled for all the events. Especially in comparison to the decay of the regional envelopes that extends over almost 3 orders on magnitude during 80 s, the slow decay of the teleseismic coda is matched by the model. Absolute amplitudes of the direct pulse show different misfit for the horizontal and vertical motion. Horizontal motion is overestimated. We attribute this to the effect of the shallow velocity structure that is not properly accounted for in our model and causes steeper incidence in reality. The vertical rotation data envelopes show larger fluctuations than translations. This is related to the lack of averaging and a higher noise level in the rotational data. The main characteristics of the data is again reproduced by the model. In contrast to the translational motion envelopes, the rotational data do not show a direct pulse due to the insensitivity of the rotation data to compressional energy. The decay is the same for rotational and translational data and is well reproduced by the model. Also the amplitude of the rotational coda envelope is well predicted by the model. This observation confirms findings of earlier studies, that the local structure and heterogeneity at the receiver side is sufficient to generate the long lasting coda of teleseismic arrivals. The model we present consistently describes the coda of regional events at variable distances and the coda of teleseismic *P*-wave arrivals including data of rotational motions. This indicates that the model correctly describes the main mechanisms generating the coda of regional and teleseismic events.

Accepting that the model provides a realistic description of the scattering process allows to investigate properties of the scattered wavefield beyond the observables that can directly be compared to measurements. The partitioning between *P* and *S* energy is one observable that is difficult to measure (Shapiro *et al.* 2000; Hennino *et al.* 2001; Margerin *et al.* 2009) in the field but can easily be simulated (Margerin *et al.* 2000). According to Ryzhik *et al.* (1996) the theoretical value for the *S*- to *P*-energy ratio for long lapse times tends to stabilize in infinite space at

$$\frac{E_S}{E_P} = \frac{2v_p^3}{v_s^3}, \tag{23}$$

with E_S and E_P being *S*- and *P*-energy, v_p and v_s are *P*- and *S*-wave speeds, respectively. This is the value that we expect to find in our simulation as the interference effect at the surface, that leads to a locally different value at the surface (Margerin *et al.* 2009), is not included in our model. The velocity structure in our model results in an equipartition ratio of 10.7. In Fig. 12, we show the temporal evolution of energy partitioning for the regional and teleseismic simulations. For the regional case we observe a fast stabilization of the partition ratio at the expected value of 10.7 only a short time after the passage of the direct *S*-wave. This behaviour is similar to simulations shown by Margerin *et al.* (2000). In contrast the simulations for the excitation by teleseismic waves converge to a *S*- to *P*-energy ratio of about 30, this is an indication that the equipartition regime is not reached even after 400 s. The ratio of 30 also indicates, that there is an excess of *S*-energy which is surprising as the teleseismic wavefield is excited by a pure *P* source. The explanation for this observation is the excitation by the plane wave impinging on the crust. To illustrate this we show the spatial distribution of deformation energy at 50 s lapse time (Fig. 13). In the case of the regional simulation (compare Fig. 4, 50 s) we observe the expected behaviour with a *S*- to *P*-energy ratio below the equipartition value
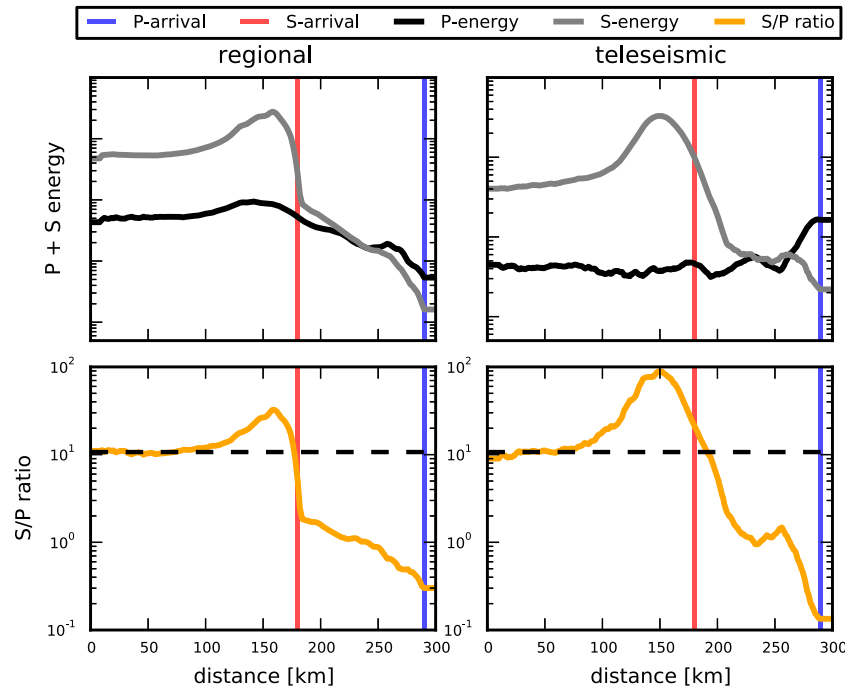
Figure 13. Spatial evolution of the equipartition ratio for *S* and *P* energy. Top row shows a temporal, space dependent snapshot of *P* and *S* energy of an regional (left-hand side) and teleseismic event (right-hand side) for a 50 s lapse time. Traces are according to the snapshots shown in Figs 4 and 6. Bottom row gives the ratio of *S* and *P* energy. Dashed black line represents the theoretical equipartition value of 10.7.

between the *P*- and *S*-wave fronts and above equipartition directly behind the *S*-wave train. Around the source location some distance behind the *S*-wave front the ratio converges towards equipartition. The illustration of the spatial energy distribution for the teleseismic excitation is related to Fig. 5. The teleseismic plane wave excitation corresponds to an areal distribution of upward directed *P* sources. Fig. 13(right-hand side) shows the energy distribution for one of these sources at 50 s lapse time. Even though this source emits pure *P* energy the figure shows that a *S* wave is generated by scattering close to the source that propagates as guided wave as seen in Fig. 6. The energy partitioning is similar to the isotropic source inside the crust in the regional simulations and converges towards the equipartition ratio of 10.7 behind the *S* wave. The integral effect of the areal distribution of such sources that makes up the plane wave excitation causes a superposition of sources at different distances. As seen in Fig. 5 the strongest contribution in this source integral comes from sources in the distance corresponding to the propagation distance of the guided *S* waves. These sources introduce an excess in *S*-wave energy which leads to an increased *S*- to *P*-energy ratio above the theoretically expected equipartition value.

7 CONCLUSIONS

We introduce a method to model multicomponent seismogram envelopes of translational and rotational motions in a deterministic, macroscopic background structure with space dependent heterogeneities. This approach is based on Monte Carlo solutions to the RTEs with multiple anisotropic scattering described in the Born approximation. Using this method we are able to model events in the regional and teleseismic distance range. The scaling of the rotations with respect to the translational motions described in eqs (15) and (17) and used in Sections 5.1 and 5.2 shows that *S* waves can locally be treated as plane waves. We obtain crustal scattering and attenuation parameters in the Vogtland region in southeast Germany using

an inversion of regional earthquake envelopes. Other studies in Europe and in Germany confirm the results. Scattering in the mantle is not required for the modelling of the envelopes, but weak scattering can not be ruled out completely. Simulations of teleseismic arrivals using an identical set of crustal scattering and attenuation parameters show a good agreement with translational and rotational motion data observed from deep teleseismic events. The observed rotations around the vertical axis indicate the scattering from *P* to *SH* energy in the vicinity of the receiver and therefore strengthen the argument of multiple scattering at 3-D heterogeneities. Observations of equipartition in the regional coda show a rapid stabilization around the theoretically expected value, while in the teleseismic *P* coda the energy partitioning favours *S* waves due to the spatially extended source mechanism of the incident plane wave.

REFERENCES

Abubakirov, I.R. & Gusev, A.A., 1990. Estimation of scattering properties of lithosphere of Kamchatka based on Monte Carlo simulation of record envelope of a near earthquake, *Phys. Earth planet. Inter.,* **64,** 52–67.

Aki, K., 1969. Analysis of the seismic coda of local earthquakes as scattered waves, *J. geophys. Res.,* **74**(2), 615–631.

Aki, K., 1980. Attenuation of shear-waves in the lithosphere for frequencies from 0.05 to 25 Hz, *Phys. Earth planet. Inter.,* **21**, 50–60.

Aki, K., 1981. Scattering and attenuation of high-frequency body waves (1–25 Hz) in the lithosphere, *Phys. Earth planet. Inter.,* **26**, 241–243.

Aki, K. & Chouet, B., 1975. Origin of coda waves: source, attenuation, and scattering effects, *J. geophys. Res.,* **80**(23), 3322–3342.

Aki, K. & Richards, P.G., 2002. *Quantitative Seismology,* University Science Books.

Bernauer, M., Fichtner, A. & Igel, H., 2009. Inferring earth structure from combined measurements of rotational and translational ground motions, *Geophysics,* **74**(6), 41–47.

Beyreuther, M., Barsch, R., Krischer, L., Megies, T., Behr, Y. & Wassermann, J., 2010. ObsPy: a Python toolbox for seismology, *Seism. Res. Lett.,* **81**(3), 530–533.

Brokešová, J., Málek, J. & Kolínský, P., 2012. Rotaphone, a mechanical seismic sensor system for field rotation rate measurements and its in situ calibration, *J. Seismol.,* **16**(4), 603–621.

Calvet, M. & Margerin, L., 2013. Lapse-time dependence of coda Q: anisotropic multiple-scattering models and application to the Pyrenees, *Bull. seism. Soc. Am.,* **103**(3), 1993–2010.

Chandrasekhar, S., 1960. *Radiative Transfer,* Dover Publications, Inc.

Dainty, A., 1981. A scattering model to explain seismic Q observations in the lithosphere between 1 and 30 Hz, *Geophys. Res. Lett.,* **8**(1), 1126–1128.

Dainty, A., Toksöz, M., Anderson, K., Nakamura, Y. & Latham, G., 1974. Seismic scattering and shallow structure of the Moon in Oceanus Procellarum, *The Moon,* **9**(1), 11–29.

Dziewonski, A.M. & Anderson, D.L., 1981. Preliminary reference Earth model, *Phys. Earth planet. Inter.,* **25**, 297–356.

Fehler, M., Hoshiba, M., Sato, H. & Obara, K., 1992. Separation of scattering and intrinsic attenuation for the Kanto-Tokai region, Japan, using measurements of S-wave energy versus hypocentral distance, *Geophys. J. Int.,* **108**(3), 787–800.

Fischer, T., Horálek, J., Hrubcová, P., Vavryčuk, V., Bräuer, K. & Kämpf, H., 2013. Intra-continental earthquake swarms in West-Bohemia and Vogtland: a review, *Tectonophysics,* **611**, 1–27.

Franke, W., 1989. Variscan plate tectonics in Central Europecurrent ideas and open questions, *Tectonophysics,* **169**(4), 221–228.

Gusev, A. & Abubakirov, I., 1987. Monte-Carlo simulation of record envelope of a near earthquake, *Phys. Earth planet. Inter.,* **49**(1–2), 30–36.

Hadziioannou, C., Gaebler, P., Schreiber, U., Wassermann, J. & Igel, H., 2012. Examining ambient noise using colocated measurements of rotational and translational motion, *J. Seismol.,* **16**(4), 787–796.

Hennino, R., Trégourès, N., Shapiro, N., Margerin, L., Campillo, M., van Tiggelen, B. & Weaver, R., 2001. Observation of equipartition of seismic waves, *Phys. Rev. Lett.,* **86**(15), 3447–3450.

Hock, S., Korn, M., Ritter, J.R.R. & Rothert, E., 2004. Mapping random lithospheric heterogeneities in northern and central Europe, *Geophys. J. Int.,* **157**(1), 251–264.

Hoshiba, M., 1995. Estimation of nonisotropic scattering in western Japan using coda waves enevelopes: application of a multiple nonisotropic scattering model, *J. geophys. Res.,* **100**, 645–657.

Hoshiba, M., Sato, H. & Fehler, M., 1991. Numerical basis of the separation of scattering and intrinsic absorption from full seismogram envelope: a Monte-Carlo simulation of multiple isotropic scattering, *Pap. Meteorol. Geophys,* **42**(2), 65–91.

Igel, H., Schreiber, U., Flaws, A., Schuberth, B., Velikoseltsev, A. & Cochard, A., 2005. Rotational motions induced by the M8.1 Tokachi-oki earthquake, September 25, 2003, *Geophys. Res. Lett.,* **32**(8), 1–5.

Igel, H., Cochard, A., Wassermann, J., Flaws, A., Schreiber, U., Velikoseltsev, A. & Pham Dinh, N., 2007. Broad-band observations of earthquake-induced rotational ground motions, *Geophys. J. Int.,* **168**(1), 182–196.

Ishimaru, A., 1978. *Wave Propagation and Scattering in Random Media,* Academic Press.

Kennett, B. & Engdahl, E., 1991. Traveltimes for global earthquake location and phase identification, *Geophys. J. Int.,* **105**, 429–465.

Klügel, T., Schreiber, U., Schneider, M., Riepl, S., Schlüter, W., Weber, H. & Stedman, G., 2001. Realisierung des Großringlasers G auf der Fundamentalstation Wettzell, Tech. rep.

Krüger, F., 1994. Sediment structure at GRF from polarization analysis of P waves of nuclear explosions, *Bull. seism. Soc. Am.,* **84**(1), 149–170.

Kurrle, D., Igel, H., Ferreira, A.M.G., Wassermann, J. & Schreiber, U., 2010. Can we estimate local Love wave dispersion properties from collocated amplitude measurements of translations and rotations?, *Geophys. Res. Lett.,* **37**(4), 1–5.

Lacombe, C., Campillo, M., Paul, A. & Margerin, L., 2003. Separation of intrinsic absorption and scattering attenuation from *Lg* coda decay in central France using acoustic radiative transfer theory, *Geophys. J. Int.,* **154**(2), 417–425.

Levander, A., Hobbs, R., Smith, S., England, R., Snyder, D. & Holliger, K., 1994. The crust as a heterogeneous optical medium, or crocodiles in the mist, *Tectonophysics,* **232**(1–4), 281–297.

Margerin, L., Campillo, M. & van Tiggelen, B., 2000. Monte Carlo simulation of multiple scattering of elastic waves, *J. geophys. Res.,* **105**, 7873–7892.

Margerin, L., Campillo, M., Van Tiggelen, B.A. & Hennino, R., 2009. Energy partition of seismic coda waves in layered media: theory and application to Pinyon Flats Observatory, *Geophys. J. Int.,* **177**(2), 571–585.

McLeod, D. & Stedman, G., 1998. Comparison of standard and ring laser rotational seismograms, *Bull. seism. Soc. Am.,* **88**(6), 1495–1503.

Mitchell, M., 1996. *An Introduction to Genetic Algorithms,* MIT Press.

Mueller, S. & Panza, G.F., 1986. Evidence of a deep-reaching lithospheric root under the Alpine Arc, in *The Origin of Arcs,* Vol. 21: Developments in Geotectonics, pp. 93–113, ed. Wezel, F.-C., Elsevier.

Pancha, A., Webb, T., Stedman, G., McLeod, D. & Schreiber, U., 2000. Ring laser detection of rotations from teleseismic waves, *Geophys. Res. Lett.,* **27**(21), 3553–3556.

Pham, N.D., Igel, H., Wassermann, J., Cochard, A. & Schreiber, U., 2009a. The effects of tilt on interferometric rotation sensors, *Bull. seism. Soc. Am.,* **99**(2B), 1352–1365.

Pham, N.D., Igel, H., Wassermann, J., Kaser, M., de la Puente, J. & Schreiber, U., 2009b. Observations and modeling of rotational signals in the P coda: constraints on crustal scattering, *Bull. seism. Soc. Am.,* **99**(2B), 1315–1332.

Przybilla, J. & Korn, M., 2008. Monte Carlo simulation of radiative energy transfer in continuous elastic random media-three-component envelopes and numerical validation, *Geophys. J. Int.,* **173**(2), 566–576.

Przybilla, J., Korn, M. & Wegler, U., 2006. Radiative transfer of elastic waves versus finite difference simulations in two-dimensional random media, *J. geophys. Res.,* **111**(B4), 1–13.

Przybilla, J., Wegler, U. & Korn, M., 2009. Estimation of crustal scattering parameters with elastic radiative transfer theory, *Geophys. J. Int.,* **178**(2), 1105–1111.

Rothert, E., 2000. Small-scale heterogeneities below the Gräfenberg array, Germany from seismic wavefield fluctuations of Hindu Kush events, *Geophys. J. Int.,* **140**, 175–184.

Ryzhik, L., Papanicolaou, G. & Keller, J., 1996. Transport equations for elastic and other waves in random media, *Wave Motion,* **24**(4), 327–370.

Sato, H., 1977. Energy propagation including scattering effects: single isotropic scattering approximation, *J. Phys. Earth,* **25**, 27–41.

Sato, H., Fehler, M.C. & Maeda, T., 2012. *Seismic Wave Propagation and Scattering in the Heterogeneous Earth,* 2nd edn, Springer-Verlag.

Schreiber, K., Velikoseltsev, A., Rothacher, M., Klügel, T., Stedman, G. & Wiltshire, D., 2004. Direct measurement of diurnal polar motion by ring laser gyroscopes, *J. geophys. Res.,* **109**(B6), B06405, doi:10.1029/2003JB002803.

Schreiber, K., Hautmann, J., Velikoseltsev, A., Wassermann, J., Igel, H., Otero, J., Vernon, F. & Wells, J., 2009. Ring laser measurements of ground rotations for seismology, *Bull. seism. Soc. Am.,* **99**(2B), 1190–1198.

Sens-Schönfelder, C. & Wegler, U., 2006. Radiative transfer theory for estimation of the seismic moment, *Geophys. J. Int.,* **167**(3), 1363–1372.

Sens-Schönfelder, C., Margerin, L. & Campillo, M., 2009. Laterally heterogeneous scattering explains Lg blockage in the Pyrenees, *J. geophys. Res.,* **114**(B7), doi:10.1029/2008JB006107.

Shapiro, N.M., Campillo, M., Margerin, L., Singh, S.K., Kostoglodov, V. & Pacheco, J., 2000. The energy partitioning and the diffusive character of the seismic coda, *Bull. seism. Soc. Am.,* **90**(3), 655–665.

Shearer, P.M. & Earle, P., 2008. Observing and modeling elastic scattering in the deep Earth, *Adv. Geophys.,* **50,** 167–193.

Shearer, P.M., 1999. *Introduction to Seismology,* Cambridge Univ. Press.

Toksöz, M.N., Dainty, A.M., Reiter, E. & Wu, R.-S., 1988. A model for attenuation and scattering in the Earth's crust, *Pure appl. Geophys.,* **128**(1–2), 81–100.

Trégourès, N., Hennino, R., Lacombe, C., Shapiro, N.M., Margerin, L., Campillo, M. & van Tiggelen, B.A., 2002. Multiple scattering of seismic waves, *Ultrasonics,* **40**(1–8), 269–274.

Turner, J.A. & Weaver, R.L., 1994. Radiative transfer of ultrasound of ultrasound, *J. acoust. Soc. Am.,* **96**(6), 3654–3674.

Vallée, M., 2013. Source time function properties indicate a strain drop independent of earthquake depth and magnitude, *Nat. Commun.,* **4,** doi:10.1038/ncomms3606.

Vallée, M., Charléty, J., Ferreira, A.M.G., Delouis, B. & Vergoz, J., 2011. SCARDEC: a new technique for the rapid determination of seismic moment magnitude, focal mechanism and source time functions for large earthquakes using body-wave deconvolution, *Geophys. J. Int.,* **184**(1), 338–358.

Weaver, R., 1990. Diffusivity of ultrasound in polycrystals, *J. Mech. Phys. Solids,* **38,** 55–86.

Wegler, U. & Lühr, B.-G., 2001. Scattering behaviour at Merapi volcano (Java) revealed from an active seismic experiment, *Geophys. J. Int.,* **145**(3), 579–592.

Wessel, P. & Smith, W.H.F., 1991. Free software helps map and display data, *EOS, Trans. Am. geophys. Un.,* **72**(41), 441–446.

Wu, R., 1985. Multiple scattering and energy transfer of seismic wavesseparation of scattering effect from intrinsic attenuation – I. Theoretical modelling, *Geophys. J. R. astr. Soc.,* **82,** 57–80.

Wu, R. & Aki, K., 1988. Multiple scattering and energy transfer of seismic waves—separation of scattering effect from intrinsic attenuation – II. Application of the theory to Hindu Kush Region, *Pure appl. Geophys.,* **128,** 49–80.

Zeis, S., Gajewski, D. & Prodehll, C., 1990. Crustal structure of southern Germany from seismic refraction data, *Tectonophysics,* **176,** 59–86.